Using multi-source data from lidar, radar, imaging spectroscopy, and national forest inventories to simulate forest carbon fluxes

Article (Accepted Version)

Using multi-source data from lidar, radar, imaging spectroscopy, and national forest inventories to simulate forest carbon fluxes

Antonarakis, A.S.[1]
Siqueira, P.[2]
Munger, J.W.[3]

[1]Department of Geography, Sussex University, Chichester 1, Falmer, Brighton, BN1 9QJ, Email: a.antonarakis@sussex.ac.uk ; Telephone: +44 (0)1273-87-3490

[2]Department of Electrical and Computer Engineering, University of Massachusetts, Amherst, MA, USA.

[3]School of Engineering and Applied Sciences, Harvard University, Cambridge, MA, USA

Abstract: Terrestrial biosphere carbon dynamics are the most uncertain elements of the global carbon budget. Carbon stocks estimated using spatially-extensive remote sensing are crucial in reducing this uncertainty, and using these stocks as initial conditions to biosphere models can improve carbon flux predictions beyond the site level. Yet remote sensing data are not always consistently available for large regions, so methods assessing carbon uncertainty using data sources in one location may not be transferable to another. This study assesses the use of multiple-source data from lidar, radar, imaging spectroscopy, and national forest inventories to derive forest structure and composition necessary to initialise the Ecosystem Demography model (ED2), and hence evaluate short-term carbon flux uncertainty over Harvard Forest, Massachusetts. ED2 was initialised using forest structure and composition derived from lidar and national forest inventories, radar and national forest inventories, lidar and imaging spectroscopy, and radar and imaging spectroscopy resulting in net ecosystem productivity uncertainty of 26.3%, 41.9%, 19.6%, and 20.2% respectively compared to ground-based forest inventory initialisations. This study uniquely offers a multitude of methods to estimate forest ecosystem state, with resulting carbon uncertainties, transferable to regions with potentially different data availability. Furthermore, in preparation for satellite radar, lidar and imaging spectrometer, this study highlights the importance of combining techniques deriving forest structure and composition at different scales, binding regional to potentially global carbon-fluxes with remote sensing, reducing this uncertainty source in global climate models (GCMs).

Keywords: Carbon Fluxes; Forest Structure and Composition; Ecosystem Modelling; Biomass; Lidar; Radar; Imaging Spectroscopy

1. Introduction

Determining terrestrial carbon stocks is essential in managing deforestation and forest degradation and in improving predictions of ecosystem changes in response to climate change (Friedlingstein *et al.* 2006, Michalak, *et al.* 2011; UN-REDD, 2011). To date, the largest uncertainties in the global carbon budget are in its terrestrial components (Schimel *et al.* 2001, Le Quéré *et al.* 2016), with predictions of ecosystem responses to climate change using terrestrial biosphere models also suffering high uncertainty (Friedlingstein *et al.* 2006; Huntzinger *et al.* 2012; Ahlström *et al.* 2012). Much of this uncertainty of terrestrial biosphere modelling comes from process and parameterization error, inaccuracies in the current model equations and model parameter values; forcing error, errors in the meteorological information; and initialisation error, errors in the initial ecosystem state. Terrestrial biosphere models can incorporate information on the current ecosystem state (Medvigy *et al*. 2009; Antonaraks *et al*. 2011), and with local climatic and edaphic information (Desai *et al*. 2010), can make predictions of carbon, water, and energy fluxes at a variety of scales. Yet, information on the initial condition has traditionally come from ground-based inventories of the plant canopy within small sample plots.

Remote Sensing instruments have the ability to indirectly estimate biomass at well resolved spatial scales (Koch 2010; Naesset *et al*. 2015; Lu *et al*. 2016). Radar has the ability to penetrate canopies of different densities depending on the wavelength of the emitted pulse. Regression techniques based on backscatter amplitudes of single or multiple polarisations, have been commonly used for forest biomass estimation (Ranson & Sun 1994; Dobson *et al.* 1995; Hoekman & Quiriones 2000; Saatchi *et al.* 2007). The accuracy of biomass estimations from radar backscatter are dependent on the wavelength (C,L,P), polarization (HH,HV,VV,VH), incidence angle, terrain and dielectric properties. L and P-band radars as opposed to C-band radars can reflect from branches, trunks, and ground, and are more suitable for high biomass stands, i.e. have better saturation capabilities in dense stands. Recent studies such as Saatchi *et al*. (2011) and Ahmed *et al.* (2014) have diverged from single polarisation and single coefficient regression equations to improve biomass accuracy. Interferometric radar, providing estimates of canopy height, has also been used to increase the accuracy of biomass estimation (Saatchi *et al*. 2011; Le Toan *et al*. 2011). Lidar has less of a saturation issue with high stand density, but can be spatially limited in both airborne and satellite platforms. Lidar instruments with their power in

vertical profiling have been used to estimate biomass. This has first been through discrete return lidar (Nelson *et al.* 1988; Means *et al.* 1999; Popescu *et al.* 2003; Asner & Mascaro 2014), based on identifying individual tree features such as treetop position and height, or by defining average height or canopy top metrics. Full waveform lidar components both from airborne and satellite platforms have also been used to estimate biomass (Drake *et al.* 2002; Lefsky *et al.* 2005; Saatchi *et al.* 2011; Baccini *et al.* 2012), using regression techniques based on height and return energy metrics such as HOME (height-of-median-energy), H100 (top of the canopy), H10 to H90 (10% to 90% of height above ground), or Lorey's height (basal-area weighted height). Studies have also been done combining lidar and radar data (Tsui *et al*. 2013; Lu *et al*. 2016), where lidar-derived biomass can act as a virtual field/validation dataset to create a wall-to-wall biomass using radar data, or by combining return signals in a regression equation. Multispectral and imaging spectrometer data have been used to determine biomass through linking with radar or lidar (e.g. Nelson *et al*. 2009; Swatantran *et al*. 2011). Imaging spectroscopy has recently emerged as a useful approach for producing more resolved estimates on ecosystem composition in the form of plant species or plant functional types (e.g. Martin *et al*. 1998; Goodenough *et al*., 2003; Kokaly *et al*. 2003; Lucas & Carter 2008).

Remote sensing has been used to test, validate or constrain output from terrestrial biosphere models. Airborne radar-derived structure has been used to initialise terrestrial biosphere models such as Zelig (Ranson *et al*. 2001) and the Sheffield Dynamic Global Vegetation Model (Le Toan *et al*. 2004) mostly as a diagnostic tool to determine where land use history was accurately represented. Airborne lidar-derived structure has been used to parameterise canopy photosynthesis models (e.g. Kotchenova *et al*. 2004, Yang *et al*. 2010, Chasmer *et al*. 2011). The Ecosystem Demography model (ED2) is a particularly powerful terrestrial biosphere model as it can simulate vegetation dynamics of individual trees of a particular size and plant functional type, incorporating the full spatially heterogeneous ecosystem state measured in forest inventories. Hurtt *et al*. (2004), Thomas *et al*. (2008), and Antonarakis et al. (2011) have used ED2 adjusting sub-tile outputs from potential vegetation runs with lidar heights, improving carbon fluxes and dynamics. Antonarakis et al. (2011) also indicated that initialisations based on biomass were better than height at estimating carbon fluxes and dynamics.

Remote sensing data are not always consistently available across large regions, so methods assessing carbon uncertainty using e.g. lidar and imaging spectroscopy in one location may not be transferable to another location with only lidar. This study assesses the use of multiple source data from lidar, radar, imaging spectroscopy and national forest inventories to derive forest structure and composition necessary to initialise the size-structured ED2 model, and hence evaluate short-term carbon flux uncertainty over Harvard Forest, Massachusetts. This study for the first time provides a multitude of methods, with resulting carbon uncertainties, which are transferable to regions with different radar, lidar, imaging spectroscopy and national forest inventory data availability. Harvard Forest is an ideal site for this investigation, due to its diverse coverage of remote sensing and field data and long-term monitoring of carbon fluxes. Furthermore, the desire to accurately assess carbon stocks and dynamics is accentuated by near future satellite instruments such as HyspIRI (Hyperspectral Infrared Imager), EnMAP (Environmental Mapping and Analysis Program), GEDI (Global Ecosystem Dynamics Investigation Lidar), IceSAT 2 (Ice, Cloud, and land Elevation Satellite 2), BIOMASS (P-band radar), and NISAR (L-band NASA-ISRO Synthetic Aperture Radar).

2. Methodology

For this study carbon flux uncertainty is assessed using initial forest conditions derived from lidar and national forest inventories, radar and national forest inventories, lidar and imaging spectroscopy, and radar and imaging spectroscopy. A full description of the initial forest condition in ED2 (see also section 2.7) requires first estimating tile-level above-ground-biomass, and then sub-tile tree density and plant functional type composition. Only a recent method by Antonarakis *et al*. (2014) fusing waveform lidar (Lid) and imaging spectroscopy (IS) was able to derive the full triad of aboveground-biomass distributions by tree size-class and plant functional type composition (called Lid&IS in this study). Radar, not providing a full vertical foliage profile, has not yet be fused with imaging spectroscopy in this way, so a second method linking active remote sensing and imaging spectroscopy was developed. First, using radar or lidar, tile-level above-ground biomass (AGB) is determined from multivariate and univariate regressions based on variables extracted from lidar, similar to e.g. Lefsky *et al.* (2005) and Baccini *et al.* (2012), or from UAVSAR L-band cross- and co-polarised radar backscatter. Then lidar or radar

AGB spatial-distributions are linked to forest composition derived using spectral mixture analysis on imaging spectroscopy and tree density defined using outputs from ED2 potential vegetation (PV) runs (called Lid-PV/IS & Rad-PV/IS in this study). A third method recognizes that for some locations, imaging spectroscopy may not be available. Here, sub-tile conditions are created by linking lidar or radar AGB spatial-distributions to tree density and forest composition from the USDA forest inventory and analysis (FIA) plots (called Lid-FIA & Rad-FIA in this study). A flowchart illustrating the methods used to derive initial conditions is presented in Figure 1. Finally, ED2 is initialised using estimates of AGB size-class distributions at three sites at Harvard Forest, Environmental Measurement Site, Hemlock, and Little Prospect Hill, to estimate short-term carbon fluxes. All estimates of AGB and carbon fluxes are compared to ground-based estimates and initialisations.

2.1 Remote Sensing Instruments

Full waveform airborne lidar measurements used in this study come from the Laser Vegetation Imaging Sensor (LVIS) (Blair *et al.* 1999), flown over the Harvard Forest in the summer of 2003 and 2009 with a resulting footprint diameter of around 20 m, an along and across track sampling of 15-25 m, and with and a 30 cm vertical and 1 m location accuracy. The imaging spectroscopy measurements come from the Airborne Visible/Infrared Imaging Spectrometer (AVIRIS) flown on 5 September 2002, acquiring measurements with a spatial resolution of 3.3 m across 224 calibrated spectral bands from 400-2500 nm (Green *et al.* 1998). Atmospheric correction and the conversion of AVIRIS radiance to reflectance was performed using the Fast Line-of-sight Atmospheric Analysis of Spectral Hypercubes (FLAASH). L-band fully polarimetric radar from JPLs UAVSAR (uninhabited aerial vehicle synthetic aperture) was collected in August 2009, with a nominal resolution of 1.66 m, at an altitude of 12.5 km, a 22 km swath, incidence angles from 25^{o} to 60^{o}, and with the incident angle information provided in 5 m pixels (0.00005556^{o}). Before deriving above-ground biomass from radar, pixel area effects from topographic variation and the incidence angle dependence of radar backscatter were removed following the methodology of Ahmed *et al.* (2014).

2.2 Study Area and Forest Inventories

Above-ground biomass (AGB) is measured in the vicinity of the three flux towers at the Harvard Forest in central Massachusetts, USA; the Environmental Measurement Site (EMS), the Hemlock (HEM), and Little Prospect Hill (LPH), as well as for the Plantation plots (Barker-Plotkin 2010). The forest is dominated by deciduous species such as red oak (*Quercus rubra*), and red maple (*Acer rubrum*). Conifer species present at the site are dominated by hemlock (*Tsuga canadensis*), red pine (*Pinus resinosa*) and white pine (*Pinus strobus*). Five plant functional types were defined according to Medvigy *et al.* (2009) as early-successional conifers (e.g. *Pinus resinosa* and *Pinus strobus)*, late-successional conifers (e.g. *Tsuga canadensis, Picea rubens, Picea glauca*), early-successional hardwoods (e.g. *Betula papyrifera, Betula populifolia, Betula lenta*), mid-successional hardwoods (e.g. *Quercus rubra, Acer rubrum, Quercus velutina, Fraxinus americana*), and late-successional hardwoods (e.g. *Fagus spp., Acer saccharum*).

The EMS censuses measure all trees larger than 10 cm in diameter at breast height (dbh) in 34 10 m radius circular plots (1.07 ha) since 1997 onwards (Munger & Wofsy 1999), with an understory census in 2005 for trees between 1-10 cm dbh. The AGB at the EMS site was 10.77 kg C m^{-2} in 2003 and around 11.55 kg C m^{-2} in 2009 of which around 77% were mid-successional hardwoods, 5% were early-successional hardwoods, 4% were late-successional hardwoods, 7% were early-successional conifers, and 7% were late-successional conifers. The HEM forest inventory (Foster & Barker-Plotkin 1999) is comprised of a single 0.72 ha rectangular plot in which all trees greater than 5 cm dbh were censused in 1990, 1999, 2009. The AGB at the HEM site was 8.47 kg C m^{-2} in 1999 and 9.00 kg C m^{-2} in 2009 of which around 18% were mid-successional hardwoods, 2% were early-successional hardwoods, 1% were late-successional hardwoods, 28% were early-successional conifers, and 51% were late-successional conifers. The LPH forest inventory (Hadley 2009) measures all trees greater than 10 cm dbh in circular plots of 6 m radius established 50, 100, and 150 m from the footprint of the flux tower from 2002, resulting in a total sample area of 0.34 ha. The area experienced a severe fire in 1957, which destroyed most trees within 200 m of the flux tower. The AGB at LPH was 4.62 kg C m^{-2} in 2003 and 4.52 kg C m^{-2} in 2009 of which around 83% were mid-successional hardwoods, 4% were early-successional hardwoods, 2% were late-successional hardwoods, 9% were early-successional conifers, and 2% were late-successional conifers. The Plantation plots (PLN) at the

Prospect Hill tract (Barker-Plotkin 2010) are 15 20 m plots set up in 2007 of which 6 were harvested by 2009. The plots are dominated by early and late successional conifers (59% and 25% respectively) with an AGB of 9.07 kg C m^{-2} in 2007 and 9.89 kg C m^{-2} for the unharvested plots. On average, the three flux tower sites changed in composition between the 2 dates by only ~1% (sd 4%). Net ecosystem productivity (NEP), gross primary productivity (GPP) and ecosystem respiration (Reco) information was available for the EMS (Urbanski, et al. 2007), HEM and LPH sites (Hadley et al. 2008). The Harvard Forest study area (Prospect Hill tract), the locations of all the plots, and the three flux towers (EMS east/ HEM center/ LPH west) are shown in Figure 2d.

AGB in forest inventory plots is calculated as in the ED2 model based on coefficients from Ter-Mikaelian and Korzukhin (1997) and from parameter optimizations in Medvigy *et al.* (2009):

$$\mathrm{AGB} = n^i(z,x) \times \sum \left(B^i_{\mathrm{leaf}}(z), B^i_{\mathrm{stem}}(z), B^i_{\mathrm{sapwood}}(z) \right), \quad \text{where} \tag{1}$$

$$B^i_{\mathrm{leaf}}(z) = \alpha_1 z^{\alpha_2} \tag{2}$$

$$B^i_{\mathrm{stem}}(z) = 0.7 \times \left(\beta_1 z^{\beta_2} \right) \tag{3}$$

$$B^i_{\mathrm{sapwood}}(z) = \left(0.7 \times B^i_{\mathrm{alive}}(z) \times {q_{\mathrm{sw}}}^i \times h \right) / \left(2 + {q_{\mathrm{sw}}}^i \times h \right) \tag{4}$$

$$B^i_{\mathrm{alive}}(z) = B^i_{\mathrm{leaf}}(z) \times \left(1 + {q_{\mathrm{fr}}}^i + {q_{\mathrm{sw}}}^i \times h \right) \tag{5}$$

Where q_{sw} is the sapwood to leaves ratio, q_{fr} is the fine roots to leaves ratio, $\alpha_1, \alpha_2, \beta_1, \beta_2$ are exponents of the power functions relating to leaf and stem biomass, $n^i(z,x)$ is the tree density (n) of tree size z of each PFT i, and h is the tree height. Values of constants related the Equations 1-5 are given in Table 1.

2.3 Above-Ground Biomass from Lidar

Above-ground biomass (AGB) is measured from waveform lidar components using single and multiple regressions. The lidar components extracted are H100, $H100^2$, H10, H25, H30, H40, HOME (height-of-median-energy), H60, H75, H90, and CANOPY_DEPTH. H10 to H100 are heights in the waveform at which the cumulative energy percentile is reached;

CANOPY_DEPTH is the height between the tree top and the smoothed last point of inflection before the ground return. The singe variable related to ground-based carbon stocks with the lowest RMSE (root-mean-square-error) is chosen for the single regression. The best multiple regression is achieved using the stepwise regression method, both backward and forward. AGB is estimated for 2003 and 2009 LVIS data, where the 2009 data was not used in the statistical training, and can therefore be considered a testing dataset.

2.4 Above-Ground Biomass from Radar

A multivariate regression approach is used to relate above-ground biomass and polarimetric backscatter. Similarly to Saatchi *et al.* (2011) the three radar polarisations (HH, HV, VV) with backscatter in decibels were related to AGB as:

$$\mathrm{AGB}^{\lambda} = \beta_0 \sigma_{\mathrm{HH}} + \beta_1 \sigma_{\mathrm{HV}} + \beta_2 \sigma_{\mathrm{VV}} + \beta_3 \tag{6}$$

Where the unknown coefficients (β_0, β_1, β_2, and β_3) and exponent (λ) are determined statistically using allometrically derived biomass values from forest inventories, and then comparing to L-band UAVSAR backscatter values (σ in dB). A secondary method is tested using the biomass-backscatter model given in Hensley *et al.* (2014) and Ahmed *et al.* (2014) as:

$$\sigma_{\mathrm{p}} = A\left(1 - e^{-B\times(\mathrm{AGB})}\right) + C \times (\mathrm{AGB})^{0.2}\, e^{-B\times(\mathrm{AGB})} \tag{7}$$

Where σ_{p} is the radar backscatter (in $m^2\ m^{-2}$) of the different polarisations and the coefficients (*A, B, C*) are determined statistically using biomass values from forest inventories. This method tested the best relationship for individual polarisations.

2.5 Forest Composition from Imaging Spectroscopy

This follows the method developed in Antonarakis *et al.* (2014) and is briefly explained here. Antonarakis *et al.* (2014) developed a non-statistically calibrated method of deriving forest structure and composition combining lidar and imaging spectroscopy, and did not explicitly deal

with AGB uncertainty. The relative abundance of the five different plant functional types (PFTs) was determined from AVIRIS using Multiple Endmember Spectral Mixture Analysis (MESMA) (Roberts *et al.* 1998). MESMA allows the number of pure pixels (end-members) initially defined as belonging to a PFT to vary during the un-mixing process on a pixel-by-pixel basis. End-members in this study were selected over ground plots whose over-story was dominated by one of the five PFTs. The resulting abundance of the different plant functional types is estimated in terms of percentages within each pixel. Plot-level errors in composition abundances were 15%, 17%, 4%, 20%, and 8% for the 5 PFTS of early and late successional conifers, and early, mid and late successional hardwoods. Site level errors at EMS, HEM, LPH, and PLN were 4%, 8%, 4%, 14%, and 7% for the five PFTs.

2.6 Above-Ground Biomass from Lidar & Imaging Spectroscopy Fusion

The relative abundance of the five different PFTs was determined as in the previous section (Section 2.5). Leaf Area Index profiles of each lidar pulse of PFT *i* and location *x* ($\mathrm{LAI}^i(h,x)$) was estimated using the lidar gap fraction ($P(h,x)$) determined from Ni-Meister *et al.* (2001) and the clumping factor (γ).

$$\mathrm{LAI}^i(h,x) = q^i(x)\left[\frac{\mathrm{d}}{\mathrm{d}h}\left(\frac{-2\ln\left(P(h,x)\right)}{\gamma^i}\right)\right] \tag{8}$$

Where $q^i(x)$ is the relative abundance of PFT i at location *x*, as estimated from the imaging spectrometer. The clumping factor for hardwood PFTs is estimated as 0.93 (Ryu *et al.* 2010), and for conifers as 0.74 (Ryu *et al.* 2010; Yang *et al.* 2010). The LAI profile for each PFT calculated from (1) are then used to estimate the stem density profile of each pulse $n^i(h,x)$:

$$n^i(h,x) = \frac{(\mathrm{LAI})^i(h,x)}{(\mathrm{SLA})^i \times B^i_{\mathrm{leaf}}(h)} \tag{9}$$

Where SLA^i and B^i_{leaf} are the specific leaf area and leaf biomass of PFT *i*. To estimate AGB, the tree density with height ($n^i(h,x)$) of each PFT *i* was translated into a corresponding diameter size distribution ($n^i(z,x)$) using the height-to-diameter function $\mathrm{DBH} = 10^{(b1 \times h + b2)}$ used in the ED2 model, where the coefficients ($b1$) and ($b2$) for each of the PFTs were defined using FIA forest

inventory measurements from Worcester County, Massachusetts. AGB is then calculated as in the ED2 model shown in Equations 1-5. Values of constants related the Equation 9 are given in Table 1. AVIRIS data from 2003 is used again to estimate AGB for the 2009 LVIS dataset, as the average changes in composition at the plot level between the 2 dates was only 4.5%.

2.7 ED2 Biosphere Model

The ED2 (Ecosystem Demography) Model is an integrated terrestrial biosphere model calculating the exchange of carbon, water, and energy, incorporating hydrology, land-surface biophysics, vegetation dynamics, and soil carbon and nitrogen biogeochemistry (Moorcroft *et al.* 2001; Medvigy *et al.* 2009). ED2 utilises a set of size- and age-structured partial differential equations that track the changing structure and composition of the plant canopy. The model is first divided into grid cells that experience the same meteorological forcing specified either from a meteorological forcing dataset or from the boundary conditions of an atmospheric model. Each grid cell is subdivided into a number of horizontal tiles representing areas of forest that share a similar vegetation canopy structure and disturbance history. Finally, the state of the above ground ecosystem is described within each tile by the density of individual trees of different sizes, for a series of plant functional types. Each plant functional type also differs in terms of its leaf physiology that results in different rates of growth and mortality and sensitivity to environmental conditions. Accordingly, to initialise the ED2 model (t_0), sub-tile level or *cohort level* individual tree size, density, and PFT information is needed (i.e. $n^i(z, a, t_0)$), as well as the *tile level*, or landscape-scale age distribution ($p(a, t_0)$) that shares a similar vegetation canopy structure and disturbance age (a). Each tile contains multiple cohorts. The landscape-scale age distribution is linked to canopy structural attributes, such as canopy height and above-ground biomass. The landscape-scale age distribution of AGB at the beginning of a simulation in ED2 can be defined as AGB $(a, t_0)p(a, t_0)$, where AGB (a, t_0) is the above-ground biomass related to the canopy-gap age at the beginning of the simulation.

2.8 AGB size-class distributions and ED2 Biosphere Model Initialisations

A flowchart illustrating the remote sensing inputs and resulting initial conditions needed to produce predictions of carbon fluxes using the ED2 biosphere model, are presented in Figure 1. Remote sensing-derived AGB values from lidar or radar in this study are considered *tile-level distributions* with space. *Cohort-level* descriptions of forest density and composition ($n^i(z,x)$) are then needed to describe the full size-class distribution necessary to initialise ED2. This is achieved, in the first instance assuming that imaging spectroscopy may not be available, using the US forest service's Forest Inventory and Analysis (FIA) plots. The FIA has an extensive network of plots across the US, with a spatial density every 5-20 km^2, in which individual stems are identified to species, diameters, and plot characteristics such as soil carbon and plot ages since last disturbance are recorded. In the vicinity of the three Harvard Forest flux towers, the nearest 3 FIA plots were extracted, resulted in 12 tiles (each plot has only 4 tiles) of around 10-12 trees (cohorts) in each tile. Forest composition is prescribed by assigning the tree species reported in the FIA to the corresponding plant functional types in ED2. The AGB is calculated from each FIA cohort and tile using Eqs 1-5 and the resulting AGB tile-level distribution was then adjusted to match the distribution of equivalent AGB values derived from the remote sensing techniques $\mathrm{AGB}_{FIA}(t_0)p_{RS}(t_0)$. These changes to the AGB distribution is reflected across size-classes and plant functional types ready for initialising the ED2 model. Simulations using this setup are called Lid-FIA & Rad-FIA.

Active remote sensing and imaging spectroscopy can derive forest structure and composition attributes. Lidar and imaging spectroscopy were fused in Antonarakis *et al*. (2014) deriving the full triad of aboveground-biomass distributions by tree size-class and plant functional type composition necessary to initialise ED2. Yet, currently radar has not been fused to imaging spectroscopy in such as way due to it needing multiple vertical profile. This means that radar-derived AGB and imaging spectroscopy-derived forest composition still lack the *cohort-level* descriptions of individual tree sizes. This is resolved in this study by using output from ED2 potential vegetation simulations. Studies like Hurtt *et al*. (2004), Thomas *et al*. (2008), and Antonarakis *et al.* (2011) obtained individual tree sizes and forest composition by running and adjusting the proportion of AGB resulting from a potential vegetation (PV) simulation – long-term simulation from a near-bare-ground state and forcing with appropriate meteorological forcing until a steady-state condition. For a potential vegetation simulation run for 250 years

(similar to the older hemlock stands at Harvard Forest) the landscape-scale age distribution at the end of that simulation $\mathrm{AGB}_{PV}(a, t_{250})p_{PV}(a, t_{250})$ can be reinitialised where the remote sensing (*RS*) AGB distribution is adjusted to match the PV AGB values $\mathrm{AGB}_{PV}(a, t_{250})p_{RS}(a, t_0)$. Yet, in this study, the resulting size-class distribution output from a potential vegetation simulation at Harvard Forest is not representative of the current forest composition, but is in fact a mono-dominant stand of early successional pines (Figure S1). Therefore for this method, the *first* step was to use current forest composition derived at the plot/tile-level within each of the three flux towers using AVIRIS imaging spectroscopy as defined in Section 2.5. The *second* step was to attribute each individual plot with cohort-level (sub-tile) descriptions of individual tree sizes using output from PV runs. Here, PV runs for 250 years were initialised from near-bareground with observed climate forcing, but with each of the 5 PFT separately. Individual PFTs rather than a combination of PFTs were chosen due to that tree size class distributions are dependent on composition, and that the resulting competition between multiple PFTs in ED2 resulted in mono-dominant stands. I.e. using the current parameterization in ED2, conifers wholly outcompeted hardwoods within 100 years of simulation, as do early-successional conifers outcompete late-successional conifers, and early-successional hardwoods outcompete mid and late successional hardwoods. This means that AVIRIS derived fractional composition would not be able to adjust a multiple-PFT PV run outputting just a mono-dominant stand. Therefore, in this second step, each plot within a flux tower site was attributed cohort level tree descriptions of individual tree sizes from a single PFT potential vegetation run, dependent on its dominant PFTs derived from AVIRIS at that location. Finally for this method, the *third* step was to adjust the distribution of AGB from all plots/tiles within a flux tower site, derived from PV runs and AVIRIS forest composition (*i*), with active remote sensing (lidar/radar) estimated AGB distributions: $AGB_{PV}^{i}\,(a, t_{250})p_{RS}(a, t_0)$. This results in an altered distribution of AGB across size-classes and plant functional types ready for initialisation in the ED2 model. Simulations using this setup are called Lid-PV/IS & Rad-PV/IS.

ED2 simulations were conducted for the Harvard Forest flux tower site EMS, HEM, LPH (excluding the Plantation plots) for a period of 6 years (2003-2009). ED2 was initialised using the various methods deriving initial forest conditions, and are compared to ground-based forest inventory initialisations. These simulations are from Lid-FIA & Rad-FIA, Lid-PV/IS & Rad-

PV/IS, and from the lidar/imaging spectroscopy (L&IS) fusion method (section 2.6). The model simulations were forced with hourly measurements of air temperature, precipitation, relative humidity, wind, pressure, and radiation taken from the Harvard Forest between 1992-2009. The soil type, depth and carbon followed the methodology of Medvigy *et al*. (2009), with the dominant soil being loamy sand, and the depth of the soil prescribed up to 4.5 m, with a free drainage lower boundary condition. The soil carbon was set to consistently be 5.8 kg C m^{-2} (Medvigy *et al*. 2009; Antonarakis *et al*. 2014). All simulations were assumed to experience the same climate forcing, the climate forcing was sequentially recycled for historical spin-ups, and all simulations had the same parameterization.

3. Results

3.1 Above-ground biomass estimates

Figure 2a-c and Table 2 present plot level comparisons of remote sensing-derived above-ground biomass and ground-based forest inventory measurements at the EMS, HEM, LPH and PLN (see Figure 2d for plot locations). The lidar single regression method estimated AGB with an RMSE of 2.56 kg C m^{-2} and an R^2 of 0.50 (2.97 kg C m^{-2} and R^2 of 0.51 in 2009). The lidar multiple regression method estimated AGB with an RMSE of 2.46 kg C m^{-2} and an R^2 of 0.54 (2.90 kg C m^{-2} and R^2 of 0.52 in 2009). The radar multiple polarisation method estimated AGB with an RMSE of 3.31 kg C m^{-2} and an R^2 of 0.37. The single polarisation radar method estimated AGB with an RMSE of 3.56 kg C m^{-2} and an R^2 of 0.28. Furthermore, Table 2 shows the equations used in deriving AGB. The lidar single regression method best estimated AGB using the H60 height metric. The lidar multiple regression method best estimated AGB using H25, HOME, and H60 height metrics. The single polarisation radar method produced the closest estimates using HV polarisation. The lidar/imaging spectroscopy fusion method estimated AGB with an RMSE of 2.57 kg C m^{-2} and an R^2 of 0.55 (2.89 kg C m^{-2} and R^2 of 0.53 in 2009).

Site level average AGB is also presented in Table 2. The lidar single and multiple regression method estimates AGB within 0.95 kg C m^{-2} (11%) and 0.76 kg C m^{-2} (9%) of the ground based estimates of 10.77, 8.47, 4.62, 9.89 kg C m^{-2} for the EMS, HEM, LPH, and PLN respectively (1.41 & 1.31 kg C m^{-2} in 2009 respectively). The radar multiple and single polarisation methods

estimate AGB within 1.33 kg C m^{-2} (15.5%) and 1.4 kg C m^{-2} (16.5%) of the ground based estimates. The lidar/imaging spectroscopy fusion method estimates AGB within 0.42 kg C m^{-2} (5%) of the ground based estimates (1.13 kg C m^{-2} in 2009).

Remote sensing AGB estimates are compared to ground-based plot AGB calculations using equations 1-5. It is recognised that these ground-based estimates in themselves may contain uncertainty in their sampling and in the allometry used. The variation of AGB in the sampling of the Harvard forest plot has a SD of 3.8 kg C m^{-2}, resulting in a 95% confidence interval of 0.8 kg C m^{-2}. Estimates of uncertainty in allometry using standard error values from Ter-Mikaelian and Korzukhin (1997) resulted in AGB RMSEs of around 1.5 kg C m^{-2}.

The spatial distribution of AGB at the Harvard Forest Prospect Hill Tract is also presented in Figure 3. Here, the lidar multiple regression method produced AGB estimates for Prospect Hill of 7.4 and 8.0 kg C m^{-2} (total 26.8 and 29.1 Gg for 2003 and 2009). The lidar single regression method (not presented in Figure 3) produced AGB estimates of 7.3 and 7.8 kg C m^{-2} (total 26.5 and 28.3 Gg for 2003 and 2009). The radar multiple and single polarisation method produced AGB estimates of 7.97 and 7.06 kg C m^{-2} (total 28.8 and 25.5 Gg). The lidar/imaging spectroscopy fusion method produced average AGB estimates of 6.21 and 6.54 kg C m^{-2} (total 22.5 and 23.7 Gg for 2003 and 2009).

AGB size class distributions used to initialise the ED2 model over the EMS, LPH, and HEM sites are presented in Figure 4. This is for the ground-based forest inventory (Fig 4a), the lidar/imaging spectroscopy fusion method (Fig 4b), the lidar multiple regression and radar multiple polarisation AGB combined with FIA size class distributions (Fig 4c,d), and the lidar and radar derived AGB combined with imaging spectroscopy-derived forest composition and tree density defined using outputs from potential vegetation runs (Fig 4e,f). Note that the lidar and radar AGB linked to output from a multiple PFT Potential Vegetation run is shown in the supplement (Figure S1), and was dominated by early successional conifer, outcompeting other PFTs within 100 years.

3.2 Carbon Fluxes

Initial conditions using lidar and national forest inventories, radar and national forest inventories, lidar and imaging spectroscopy, radar and imaging spectroscopy, and lidar fused with imaging spectroscopy methods were used to initialise ED2 terrestrial biosphere model around the three flux-tower sites at Harvard Forest. Initial conditions shown in Figure 4, were used from the 2003 results, except for the radar data which was available from 2009. Yearly net ecosystem and gross primary productivity simulated between 2003-2009 are shown in Figure 5, with RMSEs of yearly fluxes given in tables 3. Monthly RMSEs are provided in the supplement (Table S1), and initialisations using AGB size class distributions from lidar and radar linked to output from a multiple PFT Potential Vegetation run are shown in Figure S2.

The 6-year average NEP (Fig 5a-c) derived from the ground-based initialisations were 0.51, 0.35, 0.63 kg C m^{-2} y^{-1} compared to the observations for the EMS, LPH and HEM towers of 0.47, 0.37, 0.63 kg C m^{-2} y^{-1}respectively (RMSEs of 0.20-0.29 kg C m^{-2} y^{-1}, average of 0.25 kg C m^{-2} y^{-1}). Resulting Carbon fluxes between the different initialisation methods are compared to the ground-based inventory initialisation. Initialising lidar and radar AGB linked with FIA plots (Lid-FIA & Rad-FIA) resulted in a 26-42% uncertainty in NEP (RMSEs of 0.130-0.208 kg C m^{-2} y^{-1} in Table 3). Lidar and radar AGB links with potential vegetation outputs and imaging spectroscopy (Lid-PV/IS & Rad-PV/IS) resulted in a 20-23% uncertainty in NEP (RMSEs of 0.100-0.113 kg C m^{-2} y^{-1} in Table 3). The 6-year average GPP (Fig 5d-f) had similar uncertainties from the various initialisation methods. The Lid-FIA & Rad-FIA initialisation methods resulted in a 20-31% uncertainty in GPP, and the Lid-PV/IS & Rad-PV/IS initialisation methods resulted in a 15.5-18.5% uncertainty in GPP. The lidar and imaging spectroscopy fusion method (Lid&IS) resulted in a 19.5% uncertainty in NEP (RMSEs of 0.97 kg C m^{-2} y^{-1} in Table 3), and 15.5% uncertainty in GPP.

4. Discussion

This study assesses the use of multiple source data from lidar, radar, imaging spectroscopy, and national forest inventories to estimate current and predicted future carbon uncertainties at a temperate forest site. Current carbon stocks were estimated using regression methods

incorporating lidar height metrics or L-band radar polarised backscatter. This resulted in plot-level AGB within 2.46-2.56 kg C m^{-2} (30-32%) and 3.31-3.56 kg C m^{-2} (41-44%) of ground based calculations using radar and lidar, and within 0.76-0.95 kg C m^{-2} (9-12%) and 1.33-1.40 kg C m^{-2} (16-17%) at the level of the Harvard Forest flux tower sites. Lidar or radar deriving forest structure were first linked to forest composition and individual tree sizes from USDA forest inventories (Lid-FIA & Rad-FIA). Consequently, lidar or radar AGB were linked to imaging spectroscopy-derived forest composition and tree sizes output from potential vegetation simulations (Lid-PV/IS & Rad-PV/IS). The Ecosystem Demography model was then initialised using the Lid-FIA, Rad-FIA, Lid-PV/IS, and Rad-PV/IS initial conditions, resulting in NEP uncertainty of 26.3%, 41.9%, 22.8%, and 20.2% respectively compared to ground-based forest inventory initialisations. The method fusing full waveform lidar and imaging spectroscopy (Lid&IS; Antonarakis *et al*. 2014) also resulted in low uncertainty AGB estimates (plot/site level RMSE of 2.57/0.42 kg C m^{-2}), and resulting carbon fluxes within 19.6% of ground based initialisations. These results, in preparation for satellite radar (BIOMASS/NISAR), lidar (GEDI/IceSAT2) and imaging spectrometer (HyspIRI), highlight the importance of combining techniques deriving forest structure and composition, binding regional to potentially global carbon-fluxes with remote sensing, reducing this uncertainty source in Global Climate Models.

4.1 Above-ground biomass estimation

In this study, remote sensing techniques were used to estimate plot level, site level, and regional AGB. The closest plot level estimates of AGB resulted from the lidar multiple regression method (see Table 2) The closest site level estimates of AGB resulted from the lidar and imaging spectroscopy fusion method (L&IS). This follows that the lidar multiple regression method was calibrated at the plot level, while the L&IS method was manually compared to ground-based site-level data. Radar derived AGB performed worse than the other methods at both spatial scales. The L-band radar derived AGB saturates above a range from 7-8 kg C m^{-2}, comparable to the 7.5-10 kg C m^{-2} range given in Saatchi *et al*. (2011). The resulting multiple polarisation method (Equation 6 & Fig 2c) results in overestimated low biomass and underestimated high biomass values. For all methods, the AGB uncertainty decreased with a larger study area, from 30-41% over plot sizes of 115-400 m^2, to 10-16% over site sizes of 0.34-1.06 ha. Scales of forest patches between 0.25-1 ha have been shown to produce good accuracy of forest biomass using

remote sensing (Keller et al 2001; Ahmed et al. 2013; Mascaro et al. 2011; Saatchi et al. 2011), and can increase AGB accuracy by 10-38% at 1 ha or less than an RMSE 2 kg C m^{-2}. This study has predicted ecosystem dynamics at scales within this range at the three Harvard Forest flux-towers, producing ecologically significant and potentially policy-relevant results on carbon stocks and fluxes.

Above-ground-biomass, over the validation plots, increased between 2003-2009 by 0.17 and 0.26 kg C m^{-2} using the Lid/IS and lidar multiple regression methods, and 0.33 and 0.63 kg C m^{-2} considering the whole Prospect Hill region (Fig 3). The ground plots themselves showed an increase of 0.37 kg C m^{-2}. This decrease in accuracy in 2009 (Table 2 and Figure 2) and the underestimation of AGB change, may be a result of training and testing accuracies, but may also be a result of a disturbance around Harvard Forest. This disturbance comes in the form of an ice storm in December 2008. The ice storm did bring mortality among ageing red pines, but did less visible damage to other species, namely through destruction to their canopy. The amount of measured coarse and fine woody debris for 2008 was similar to the three preceding years (around 0.1 kg C m^{-2}), resulting in a decrease in 2008 LAI of around 0.86 m^2 m^{-2} (Werden *et al*. 2010). Lidar returns from within the canopy are sensitive to changes in LAI and foliage, which may have erroneously decreased AGB in some stands due to foliage loss.

The lidar multiple regression method estimated 26.8 Gg of carbon regionally in 2003 (Figure 3), similar to the radar methods (28.84 Gg of carbon). The Lid/IS method produces the lowest regional AGB estimates in 2003 of 22.5 Gg of carbon. For ground-based plots above 7.5 kg C m^{-2}, the Lid/IS, lidar and radar methods underestimated AGB by 1.01, 0.89, 1.34 kg C m^{-2}, (RMSEs of 3.08, 2.65, 3.53 kg C m^{-2}), whereas for ground-based plots below 7.5 kg C m^{-2} the Lid/IS, lidar and radar methods overestimated AGB by 0.38, 1.33, 2.36 kg C m^{-2}, (RMSEs of 1.49, 2.14, 2.95 kg C m^{-2}). This overestimation of low values may result in inflated regional AGB estimates for the lidar and radar regression methods.

4.2 Carbon Fluxes

Initialising the ED2 model with both remote sensing constrained forest structure and composition estimates results in NEP values close to ground-based initialised fluxes (Figure 5a,b,c and Table

3). Specifically, resulting NEP from the Lid-PV/IS & Rad-PV/IS runs were within 22.8% and 20.2% of ground-based initialisations respectively. Resulting NEP after initialising the lidar or radar derived AGB with FIA (Lid-FIA & Rad-FIA) were within 26% and 42% of ground-based initialisations respectively. Using FIA to infer forest composition resulted in an overestimation of late-successional conifers, especially at LPH by 35%, as well as overestimating AGB using both lidar and radar. This larger AGB combined with larger foliage density for late-successional conifers results in an increase in leaf area index at LPH (4.40 $m^2 m^{-2}$ compared to ground-based estimates of 2.83 $m^2 m^{-2}$), which increases NEP (see Fig 5b) and increases uncertainty (80-95%). Concerning HEM, the Lid-PV/IS and Rad-PV/IS initialisations performed worse than Lid-FIA and Rad-FIA initialisations due to an overabundance of estimated early-successional conifers which in this case results in a lower leaf area and lower productivity (Figure 5 c,f). Furthermore, the Rad-PV/IS initialised fluxes actually result in comparable NEP uncertainty to the Lid-PV/IS initialised fluxes even if the AGB derived from lidar is closer to observations (Table 2: RMSE 0.76 compared to 1.33 kg C m^{-2}). This can be explained by the negative skewing in size-class distributions shown in Figure 4e,f to the larger size classes. In ED2, the total leaf biomass for each PFT is capped at a 15 m in height avoiding exponentially large leaf areas for large trees. The Rad-PV/IS size class distributions are more negatively skewed than the Lid-PV/IS ultimately resulting in close total leaf biomass and LAI.

From Figure 5 it can be seen that ground-based initialised fluxes are not directly in line with the observed fluxes, with more marked differences in the GPP values for the three sites. This demonstrates the need for model process and parameter error reduction through optimization strategies, for example improving parameterizations of photosynthetic and decomposition processes. Compared to flux tower observations at Harvard Forest, the Lid&IS method estimated NEP with an RMSE of around 0.274 kg C $m^{-2} y^{-1}$ (55% uncertainty), the Lid-PV/IS and Rad-PV/IS initialisations estimated NEP with an RMSE of 0.276-0.277 kg C $m^{-2} y^{-1}$ (57% uncertainty), and the Lid-FIA and Rad-FIA initialisations estimated NEP with an RMSE of 0.284-0.302 kg C $m^{-2} y^{-1}$ (58-62% uncertainty). These are comparable to ground-based initialisations (RMSE of 0.25 kg C $m^{-2} y^{-1}$ or 49% uncertainty).

5. Conclusion

This study for the first time compares methods deriving initial forest conditions assessing their resulting current and predicted carbon uncertainties, which are transferable to regions with different data availability, i.e. radar, lidar, imaging spectroscopy, and national forest inventories. The accurate estimation of current and future forest carbon beyond flux-tower footprints, requires efforts integrating available remote sensing datasets and forest inventories with ecosystem models. This need for uncertainty reduction in carbon estimates is especially urgent to meet national and local requirements of carbon mitigation agreements (Poulter *et al*. 2015). The first explicit biomass satellite mission, BIOMASS (Le Toan *et al*. 2011), has stated maximum AGB error requirements between 70ºN and 56ºS and within pixels of 200 m, of 20% or 0.5 kg C m^{-2} for AGB < 2.5 kg C m^{-2}. This follows the need to reduce uncertainty in the land component of the global carbon budget (±22% in Pan *et al*. 2011and ±29% in Le Quéré 2016). The knock-on implications of carbon stock uncertainty on carbon flux predictions is not well-know. A recent study by Antonarakis (2014) showed at Harvard Forest, that the uncertainty in NEP is linear with the uncertainty in forest structure, i.e. a 5, 10, 20, 50% error in forest structure resulted in 5, 12, 21, 52% error in NEP. An uncertainty in the forest composition adds to the resulting NEP uncertainty. In this study, the forest composition uncertainty from imaging spectroscopy was around 8% (see section 2.5). Using FIA, the forest composition uncertainty rose to 23%. Using FIA plots, even if not directly underlying remote sensing pixels, can be valuable as they provide current tree size distributions and PFTs in a 5-10 km^2 area, yet cannot adequately describe composition heterogeneity within a 5-10 km^2 area (e.g. HEM and EMS). Therefore, if imaging spectroscopy is available as opposed to using FIA-based composition, combining remote sensing techniques deriving current forest structure and composition can further reduce carbon flux uncertainty by up to 22% as shown in this study.

The lidar and imaging spectroscopy fusion method developed in Antonarakis *et al*. (2014) provides the closest estimates of both current and future carbon fluxes, due to the combination of reduced uncertainty in deriving forest structure and composition. Yet, this relies on co-spatial imaging spectroscopy and full waveform lidar, which is currently limited for both airborne and satellite platforms. Radar used in this study was UAVSAR which is an L-band instrument, and it is recognised that better biomass estimates may come from a P-band radar instrument or from a combination of P-band backscatter with radar interferometry (Le Toan *et al.* 2011).

Interferometric radar providing a vertical canopy profile could be used in fusion with imaging spectroscopy to develop a full description of forest ecosystems as in Antonarakis *et al*. (2014). Accurately assessing regional to continental and global scale carbon stocks hinges on a) the availability of near-future satellite instruments such as HyspIRI, EnMAP, GEDI, IceSAT 2, and BIOMASS, and b) the success of observing and deriving metrics in different ecosystems from dense biodiverse tropical forests, to sparsely populated temperate and tropical savannas. These various techniques and methodologies presented in this study will prove important in constraining multi-scale estimates of current carbon stocks and how these terrestrial ecosystems will change in the future.

Acknowledgements

The authors thank Audrey Barker-Plotkin, Julian Hadley, David Forester, Paul Moorcroft, Steve Wofsy, Razi Ahmed, and the Harvard Forest LTER for their generosity in providing advice, ground-based inventories, eddy-flux tower and meteorological data.

References

Ahlström, A., Schurgers, G., Arneth, A., Smith, B. (2012). Robustness and uncertainty in terrestrial ecosystem carbon response to CMIP5 climate change projections. *Environmental Research Letters*, **7**, 044008.

Ahmed, R., Siqueira, P., Hensley, S., (2013). A study of forest biomass estimates from LiDAR in the northern temperate forests of New England. *Remote Sensing of Environment*, **130**, 21-135.

Ahmed, R., Siqueira, P., Hensley, S. (2014). Analyzing the uncertainty of biomass estimates from L-band Radar backscatter over the Harvard and Howland Forests, *IEEE Transactions on Geoscience and Remote Sensing*, **52**, 3568-3586.

Antonarakis, A.S., Saatchi, S.S., Chazdon, R.L., Moorcroft, P.R. (2011). Using Lidar and Radar measurements to constrain predictions of forest ecosystem structure and function. *Ecological Applications,* **21**, 1120-1137.

Antonarakis, A.S., Munger, J.W., Moorcroft, P.R. (2014). Imaging Spectroscopy- and Lidar-derived Estimates of Canopy Composition and Structure Improve Predictions of Forest Carbon Fluxes and Ecosystem Dynamics, *Geophysical Research Letters*, **41** (7), 2535-2542.

Antonarakis, A.S., (2014). Uncertainty in initial forest structure and composition when predicting carbon dynamics in a temperate forest. *Ecological Modelling*, **291**, 134-141.

Asner, G. P., and J. Mascaro. (2014). Mapping Tropical Forest Carbon: Calibrating Plot Estimates to a Simple LiDAR Metric. *Remote Sensing of Environment*, **140**: 614–624.

Baccini, A. *et al.* (2012). Estimated carbon dioxide emissions from tropical deforestation improved by carbon-density maps. *Nature Climate Change*, **2**, 182-185.

Barker-Plotkin, A. 2010. Plantation Biodiversity Plots at Harvard Forest since 2007. Harvard Forest Data Archive: HF162.

Blair, J.B., Rabine, D.L., Hofton, M.A. (1999). The laser vegetation imaging sensor (LVIS): A medium-altitude, digitations-only, laser altimeter for mapping vegetation and topography. *ISPRS Journal of Photogrammetry and Remote Sensing*, **54**, 115-122.

Chasmer, L., N. Kljun, C. Hopkinson, S. Brown, T. Milne, K. Giroux, A. Barr, K. Devito, I. Creed, and R. Petrone. (2011). Characterizing vegetation structural and topographic characteristics sampled by eddy covariance within two mature aspen stands using lidar and a flux footprint model: Scaling to MODIS. *Journal of Geophysical Research-Biogeosciences*, 116.

Desai, A.R., (2010). Climatic and phenological controls on coherent regional interannual variability of carbon dioxide flux in a heterogeneous landscape. *Journal of Geophysical Research: Biogeosciences*, 115(G3).

Drake, J.B., Dubayah, R.O., Clark, D.B., Knox, R.G., Blair, J.B., Hofton, M.A., Chazdon, R.L., Weishampel, J.F., Prince, S.D. (2002). Estimation of tropical forest structural characteristics using large-footprint lidar, *Remote Sensing of Environment*, **79**, 305-319.

Dobson, M. C., Ulaby, F. T., Pierce, L. E., Sharik, T. L., Bergen, K. M., Kellndorfer, J., *et al.* (1995), Estimation of Forest Biophysical Characteristics in Northern Michigan with SIR-C/X-SAR. *IEEE Transactions on Geoscience and Remote Sensing*, **33**, 877-895.

Foster D, Barker-Plotkin A. (1999). Hemlock Mapped Tree Plot. Harvard Forest Data Archive: HF031.

Friedlingstein, P, *et al.* , (2006). Climate–Carbon Cycle Feedback Analysis: Results from the C4MIP Model Intercomparison. *Journal of Climate*, **19**, 3337-3353.

Goodenough, D.G., Dyk, A., Niemann, K.O., Pearlman, J.S., Hao Chen, Tian Han, Murdoch, M., and West, C. (2003). Processing hyperion and ali for forest classification. *IEEE Transactions on Geoscience and Remote Sensing*, **41**, 1321–1331.

Green, R.O., Eastwood, M.L., Sarture, C.M., Chrien, T.G., Aronsson, M., Chippendale, B.J., Faust, J.A., Pavri, B.E., Chovit, C.J., Solis, M., Olah, M.R., Williams, O. (1998). Imaging Spectroscopy and the Airborne Visible/Infrared Imaging Spectrometer (AVIRIS). *Remote Sensing of Environment*, 65, 227-248.

Hadley J. (2009). HEM and LPH Towers - Tree Growth and Above-Ground Biomass. Harvard Forest Data Archive: HF149.

Hadley, J. L., Kuzeja, P.S., Daley, M.J., Phillips, N.G., Mulcahy, T., Singh, S. (2008). Water use and carbon exchange of red oak- and eastern hemlock-dominated forests in the northeastern U.S.: Implications for ecosystem-level effects of the hemlock woolly adelgid. *Tree Physiology,* **28**, 614-627.

Hensley, S., Oveisgharan, S., Saatchi, S., Simard, M. Ahmed, R., Haddad, Z. (2014). An Error Model for Biomass Estimates Derived From Polarimetric Radar Backscatter. *IEEE Transactions on Geoscience and Remote Sensing*, **52**, 4065-4081.

Hoekman, D.H., Quiriones, M.J.(2000). Land cover type and biomass classification using AirSAR data for evaluation of monitoring scenarios in the Colombian Amazon, *Geoscience and Remote Sensing*, **38**, 685 - 696.

Huntzinger, D.N., *et al.* (2012). North American Carbon Program (NACP) regional interim synthesis: Terrestrial biospheric model intercomparison. *Ecological Modelling*, **232**, 144-157.

Hurtt, G. C., R. Dubayah, J. Drake, P. M. Moorcroft, S. W. Pacala, J. B. Blair, and M. G. Fearon. (2004). Beyond potential vegetation: combining Lidar data and a height-structured model for carbon studies. *Ecological Applications,* 14:873-883.

Keller, M., M. Palace, and G. Hurtt. (2001). Biomass Estimation in the Tapajos National Forest, Brazil: Examination of Sampling and Allometric Uncertainties. *Forest Ecology and Management* **154**: 371–382.

Koch, B. (2010). Status and future of laser scanning, synthetic aperture radar and hyperspectral remote sensing data for forest biomass assessment. *ISPRS Journal of Photogrammetry and Remote Sensing*, **65**(6), pp.581-590.

Kokaly, R.F., Despain, D.G., Clark, R.N., and Livo, K.E. (2003). Mapping vegetation in Yellowstone National Park using spectral feature analysis of AVIRIS data. *Remote Sensing of Environment*, **84**, 437–456.

Kotchenova, S. Y., X. D. Song, N. V. Shabanova, C. S. Potter, Y. Knyazikhin, and R. B. Myneni. (2004). Lidar remote sensing for modeling gross primary production of deciduous forests. *Remote Sensing of Environment,* 92, 158-172.

Lefsky, M.A., Harding, D.J., Keller, M., Cohen, W.B., Carabajal, C.C., Espirito-Santo, F.B., Hunter, M.O., de Oliveira. (2005). Estimates of forest canopy height and aboveground biomass using ICESat. *Geophysical Research Letters*, **32**, L22S02.

Le Quéré, C., *et al.* (2016). Global carbon budget 2016. *Earth Syst. Sci. Data Discuss*., **8**, 605–649.

Le Toan, T., S. Quegan, I. Woodward, M. Lomas, N. Delbart, and G. Picard. (2004). Relating radar remote sensing of biomass to modeling of forest carbon budgets. *Climate Change*, 67, 379–402.

Le Toan, T., Quegan, S., Davidson, M. W. J., Balzter, H., Paillou, P., Papathanassiou, K., & Ulander, L. (2011). The BIOMASS mission: Mapping global forest biomass to better understand the terrestrial carbon cycle. *Remote sensing of environment*, **115**(11), 2850-2860.

Lu, D., Chen, Q., Wang, G., Liu, L., Li, G. and Moran, E., 2016. A survey of remote sensing-based aboveground biomass estimation methods in forest ecosystems. *International Journal of Digital Earth*, **9**(1), pp.63-105.

Lucas, K.L. and Carter, G.A., (2008). The use of hyperspectral remote sensing to assess vascular plant species richness on Horn Island, Mississippi. *Remote Sensing of Environment*, **112**, 3908-3915.

Martin, M.E., Newman, S.D., Aber, J.D., and Congalton, R.G. (1998). Determining forest species composition using high spectral resolution remote sensing data. *Remote Sensing of Environment*, **65**, 249–254.

Mascaro, J., M. Detto, G. P. Asner, and H. C. Muller-Landau. (2011). Evaluating Uncertainty in Mapping Forest Carbon with Airborne LiDAR. *Remote Sensing of Environment* **115** (12): 3770–3774.

Means, J. E., Acker, S. A., Harding, D. J., Blair, J. B., Lefsky, M. A., Cohen, W. B., *et al.* (1999). Use of large-footprint scanning airborne lidar to estimate forest stand characteristics in the Western Cascades of Oregon. *Remote Sensing of Environment*, **67**(3), 298–308.

Medvigy, D., Wofsy, S.C., Munger, J.W., Hollinger, D.Y., Moorcroft, P.R. (2009). Mechanistic scaling of ecosystem function and dynamics in space and time: Ecosystem Demography model version 2. *Journal of Geophysical Research*. **114**, G01002.

Michalak, A.M., Jackson, R.B., Marland, G., Sabine C.L. and the Carbon Cycle Science Working Group (2011). A U.S. Carbon Cycle Science Plan. United States Carbon Cycle Carbon Planning.

Moorcroft, P.R., Hurtt, G. C., Pacala, S. W. (2001). A Method for Scaling Vegetation Dynamics: The Ecosystem Demography Model (ED). *Ecological Monographs*, **71** (4), 557-585.

Munger W, Wofsy S. (1999). EMS - Biomass Inventories. Harvard Forest Data Archive: HF069.

Næsset, E., Bollandsås, O.M., Gobakken, T., Solberg, S. and McRoberts, R.E., 2015. The effects of field plot size on model-assisted estimation of aboveground biomass change using multitemporal interferometric SAR and airborne laser scanning data. *Remote Sensing of Environment*, **168**, 252-264.

Nelson, R., Krabill, W., & Tonelli, J. (1988). Estimating forest biomass and volume using airborne laser data. *Remote Sensing of Environment*, **24**, 247–267.

Nelson, R., K. J. Ranson, G. Sun, D. S. Kimes, V. Kharuk, and P. Montesano. (2009). Estimating Siberian Timber Volume Using MODIS and ICESat/GLAS. *Remote Sensing of Environment* 113 (3): 691–701.

Ni-Meister, W., Jupp, D.L.B., and Dubayah, R. (2001). Modeling Lidar Waveforms in Heterogeneous and Discrete Canopies. *IEEE Transactions on Geoscience and Remote Sensing*, **39**, 1943-1958.

Pan, Y., Birdsey, R.A., Fang, J., Houghton, R., Kauppi, P.E., Kurz, W.A., Phillips, O.L., Shvidenko, A., Lewis, S.L., Canadell, J.G. and Ciais, P., (2011). A large and persistent carbon sink in the world's forests. *Science*, **333**(6045), 988-993.

Popescu, S.C., R.H. Wynne, R.H. Nelson (2003). Measuring individual tree crown diameter with LIDAR and assessing its influence on estimating forest volume and biomass, *Canadian Journal of Remote Sensing*, **29** (5).

Poulter, B., Ciais, P., Joetzjer, E., Maignan, F., Luyssaert, S. and Barichivich, J., (2015), December. Reducing uncertainty for estimating forest carbon stocks and dynamics using integrated remote sensing, forest inventory and process-based modeling. In *AGU Fall Meeting Abstracts*.

Ranson, K.J., Sun, G. (1994). Mapping biomass of a northern forest using multifrequency SAR data. *IEEE Transactions on Geoscience and Remote Sensing*, **32**, 388-396.

Ranson, K. J., G. Sun, R. G. Knox, E. R. Levine, J. F. Weishampel, and S. T. Fifer. (2001). Northern forest ecosystem dynamics using coupled models and remote sensing. *Remote Sensing of Environment*, 75:291–302.

Roberts, D. A., Gardner, M.; Church R., Ustin, S. Scheer, G. & Green, R. O., (1998). Mapping Chaparral in the Santa Monica Mountains using multiple endmember spectral mixture models. *Remote Sensing of Environment*, **65**, 267-279.

Ryu, Y., Nilson, T., Kobayashi, H., Sonnentag, O., Law B.W., Baldocchi, D.D. (2010). On the correct estimation of effective leaf area index: Does it reveal information on clumping effects? *Agricultural and Forest Meteorology*, 150, 463-472.

Saatchi, S.S., Houghton, R.A., Alvala, R.C.D.Sa., Soares, J.V., Yu, Y. (2007). Distribution of aboveground live biomass in the Amazon basin. *Global Change Biology*, **13**, 816-837.

Saatchi, S.; Marlier, M.; Chazdon, R.L.; Clark, D.B.; Russell, A.E. (2011). Impact of spatial variability of tropical forest structure on radar estimation of aboveground biomass. *Remote Sens. Environ.*, **115**, 2836–2849.

Schimel, D.S. *et al.* (2001). Recent patterns and mechanisms of carbon exchange by terrestrial ecosystems. *Nature*, 414, 169-172.

Swatantran, A., Dubayah, R., Roberts, D., Hofton, M. and Blair, J.B., (2011). Mapping biomass and stress in the Sierra Nevada using lidar and hyperspectral data fusion. *Remote Sensing of Environment*, **115**(11), 2917-2930.

Ter-Mikaelian, M.T., Korzukhin, M.D. (1997). Biomass equations for sixty-five North American tree species, *Forest Ecology and Management*, **97**, 1–24.

Thomas, Q.R., Hurtt, G.C., Dubayah, R., Schilz, M.H. (2008). Using lidar data and a height-structured ecosystem model to estimate forest carbon stocks and fluxes over mountainous terrain, *Canadian Journal of Remote Sensing*, 34, S351-S363.

Tsui, O. W., N. C. Coops, M. A. Wulder, and P. L. Marshall. (2013). Integrating Airborne LiDAR and Space-borne Radar Via Multivariate Kriging to Estimate Above-ground Biomass. *Remote Sensing of Environment*, **139**, 340–352.

UN-REDD (2011). UN REDD Programme Strategy. 2011-2015.

Urbanski, S. P., Barford, C. C., Wofsy, S. C., Kucharik, C. J., Pyle, E. H., Budney, J., McKain, K., Fitzjarrald, D. R., Czikowsky, M. J., Munger, J. W. (2007). Factors controlling CO2 exchange on time scales from hourly to decadal at Harvard Forest. *Journal of Geophysical Research-Biogeosciences*, **112**, G02020.

Werden, L. K., Connell, T. L. Sanchez, L. K., Wofsy, S. C., and Munger, J. W. (2010). Quantifying the Impact of an Ice Storm on the Carbon Budget of a Mixed Deciduous Forest in Central Massachusetts. Harvard Forest Symposium Abstract 2010.

Yang, W., W. Ni-Meister, N.Y. Kiang, P.R. Moorcroft, A.H. Strahler, and A. Oliphant, 2010: A clumped-foliage canopy radiative transfer model for a global dynamic terrestrial ecosystem model. II: Comparison to measurements. *Agr. Forest Meteorol*., 150, 895-907.

Table 1. Plant Functional Type attributes: specific leaf area (SLA), and the allometric coefficients of the diameter-leaf biomass (B_{leaf}), diameter stem biomass (B_{stem}) , and height-to-dbh relationships as well as the ratios of sapwood (q_{sw}) and fineroots (q_{fr}) to leaves. Height-to-dbh takes the form DBH = 10^($b1$*H+$b2$). Information is from Antonarakis et al. (2014) and Medvigy et al. (2009).

Attribute	Early-successional conifer	Late-successional conifer	Early-successional hardwood	Mid-successional hardwood	Late-successional hardwood
SLA (m^2 $kg^{-1}C^{-1}$)	6	10	30	24	60
B_{leaf} exponent α_1	0.024	0.045	0.0031	0.0148	0.0085
B_{leaf} coefficient α_2	1.899	1.683	2.249	1.86	1.731
B_{stem} exponent β_1	0.073	0.081	0.013	0.081	0.117
B_{stem} coefficient β_2	2.238	2.154	2.960	2.457	2.252
q_{sw} [$kg_{sapwood}$ kg_{leaves}^{-1}]	0.00154	0.00256	0.00769	0.00621	0.0154
q_{fr} [$kg_{fineroot}$ kg_{leaves}^{-1}]	0.346	0.346	1.127	1.127	1.127
Height-DBH slope b_1	0.033	0.032	0.044	0.048	0.029
Height-DBH intercept b_2	0.827	0.969	0.568	0.519	0.826

Table 2. Above-ground biomass plot level and site level estimated from the various remote sensing methods showing equations and R^2 and RMSE values. Site level RMSEs are the scale of the flux-tower footprints. Values in parentheses are for the 2009 calculations of AGB using lidar, where 2009 data were not used in the statistical training.

Method	AGB equation	Plot R^2	Plot RMSE (kg C m^{-2})	Site RMSE (kg C m^{-2})
Lidar/ImSpec Fusion		0.55 (0.53)	2.57 (2.89)	0.42 (1.13)
Lidar single	0.914 x (H60)-8.519	0.50 (0.51)	2.56 (2.97)	0.95 (1.41)
Lidar multiple	0.369 x (H25)-1.122 x (HOME)+1.785 x (H60)-9.800	0.54 (0.52)	2.46 (2.90)	0.76 (1.31)
Radar	$AGB^{1.2}=1.51\sigma_{HH}+1.83\sigma_{HV}-0.55\sigma_{VV}+42.12$	0.37	3.31	1.33
Radar2	$\sigma_{HV}=0.402 \times (1-e^{-0.0199 \times (AGB)})+0.006 \times (AGB)^{0.2} \times e^{-0.0199 \times (AGB)}$	0.28	3.56	1.40

Table 3. Yearly net ecosystem and gross primary productivity RMSEs from the ground inventory-initialisations, predicted at the scale of the EMS, HEM and LPH flux-tower footprints for the various initialisation methods Lid&IS (Lidar and Imaging Spectroscopy fusion), Lid-FIA & Rad-FIA (Lidar and Radar AGB links with FIA), and Lid-PV/IS & Rad-PV/IS (Lidar and Radar AGB links with potential vegetation outputs and imaging spectroscopy).

	GPP RMSE (kg C m^{-2} yr^{-1})				NEP RMSE (kg C m^{-2} yr^{-1})			
Method	**EMS**	**LPH**	**HEM**	**All sites**	**EMS**	**LPH**	**HEM**	**All sites**
Lid&IS fusion	0.063	0.477	0.219	**0.253**	0.021	0.219	0.051	**0.097**
Lid-FIA	0.143	0.720	0.148	**0.337**	0.049	0.277	0.065	**0.130**
Rad-FIA	0.427	0.860	0.282	**0.523**	0.155	0.331	0.138	**0.208**
Lid-PV/IS	0.239	0.044	0.659	**0.314**	0.085	0.036	0.218	**0.113**
Rad-PV/IS	0.148	0.030	0.602	**0.260**	0.055	0.051	0.194	**0.100**

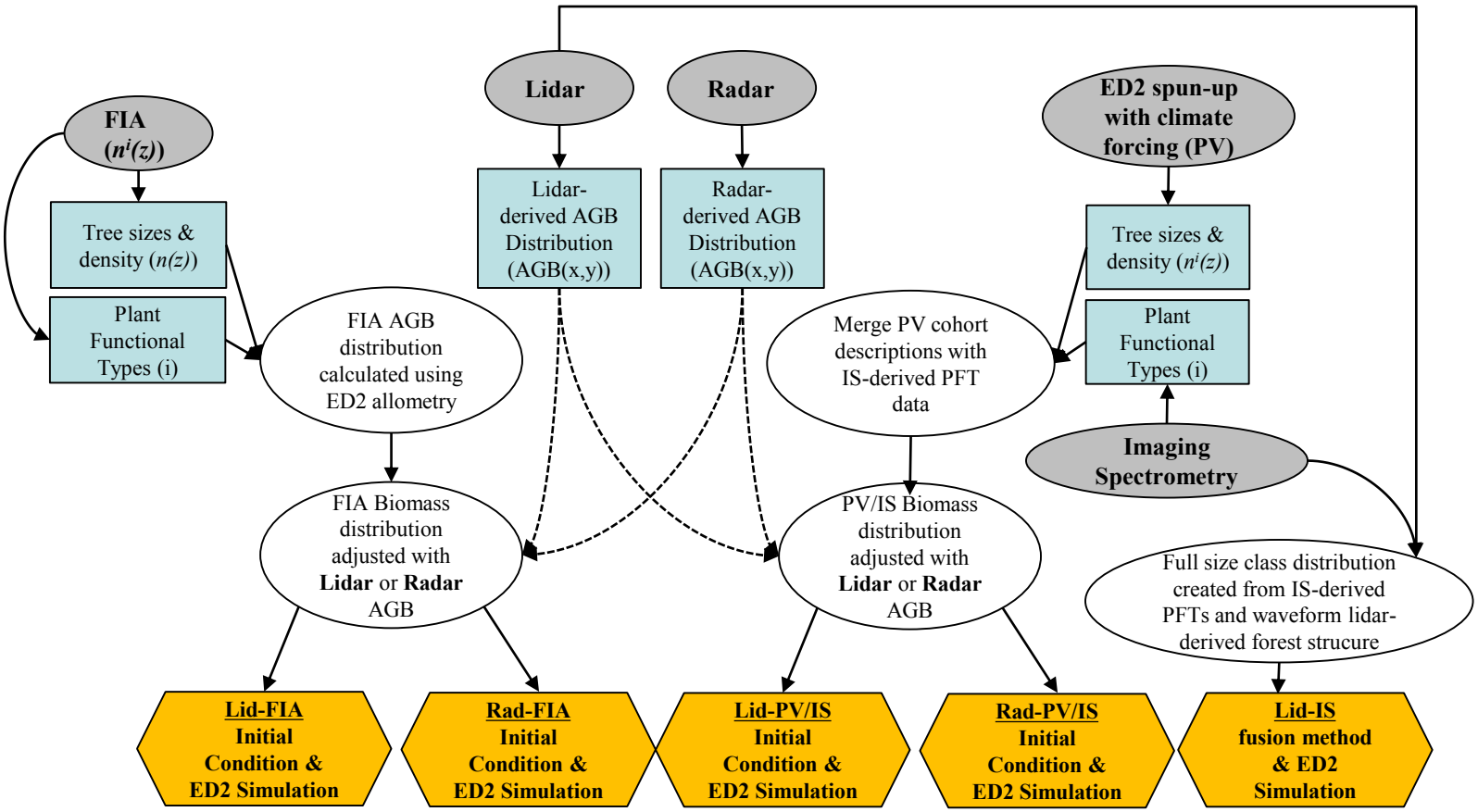

Figure 1.Flowchart illustrating the inputs and initial conditions needed to produce predictions of carbon fluxes using the ED2 biosphere model. These are through integrating Radar, Lidar, FIA, potential vegetation simulations, and imaging spectroscopy data to produce initial conditions.

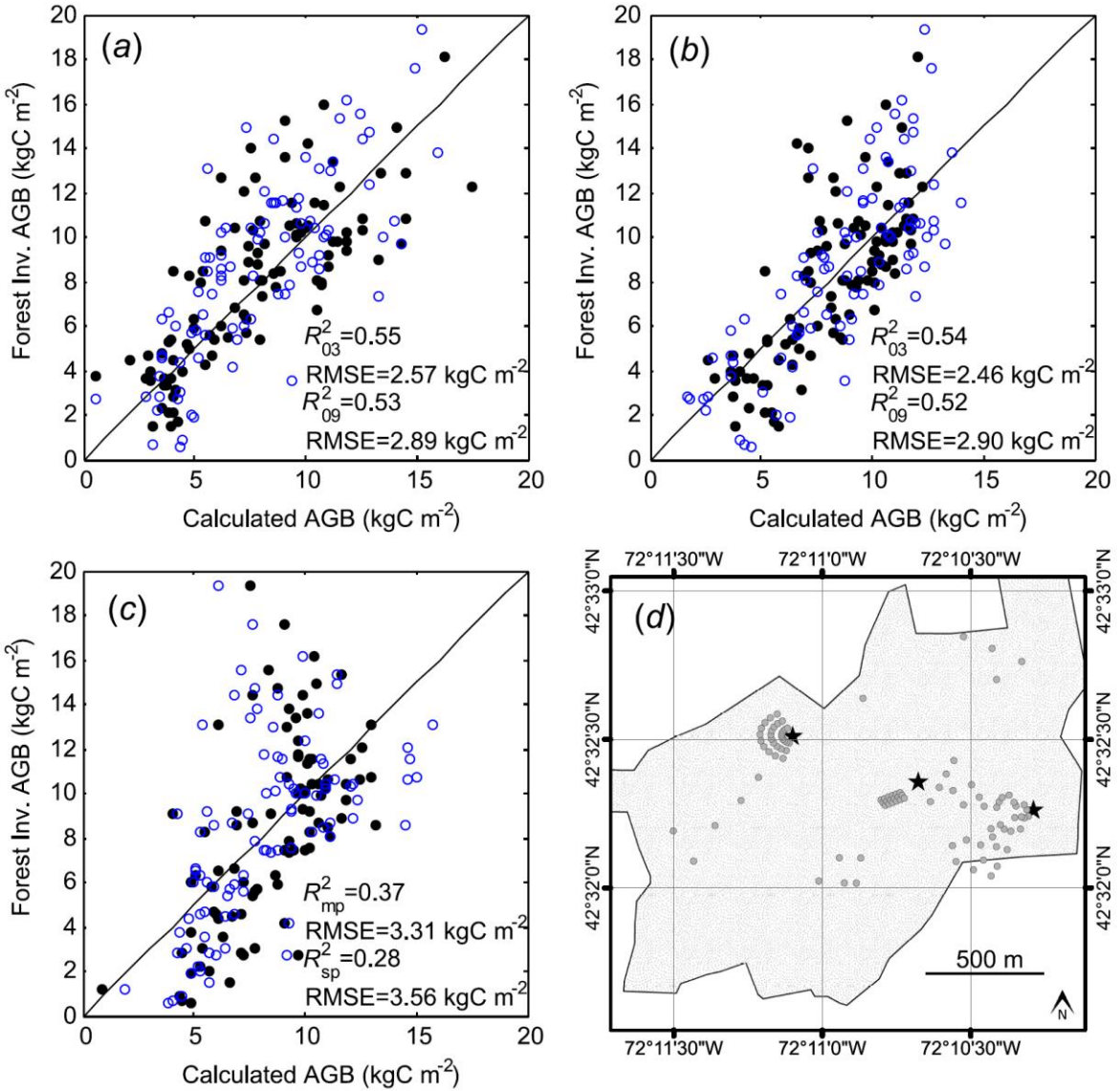

Figure 2. Remote-sensing derived estimates of AGB compared to ground-based measurements. These are for the EMS, HEM, LPH, and PLN plots. Panel a) shows results from the Lidar and imaging spectroscopy fusion method of deriving AGB between 2003 (closed circles) and 2009 (open circles); b) shows results from the Lidar multiple regression method; c) results from UAVSAR using the multiple polarisation (closed circles) and single polarisation (open circles) method. Panel d) shows the Harvard Forest study area (Prospect Hill tract), the locations of all the plots, and the three flux towers (EMS east/ HEM center/ LPH west).

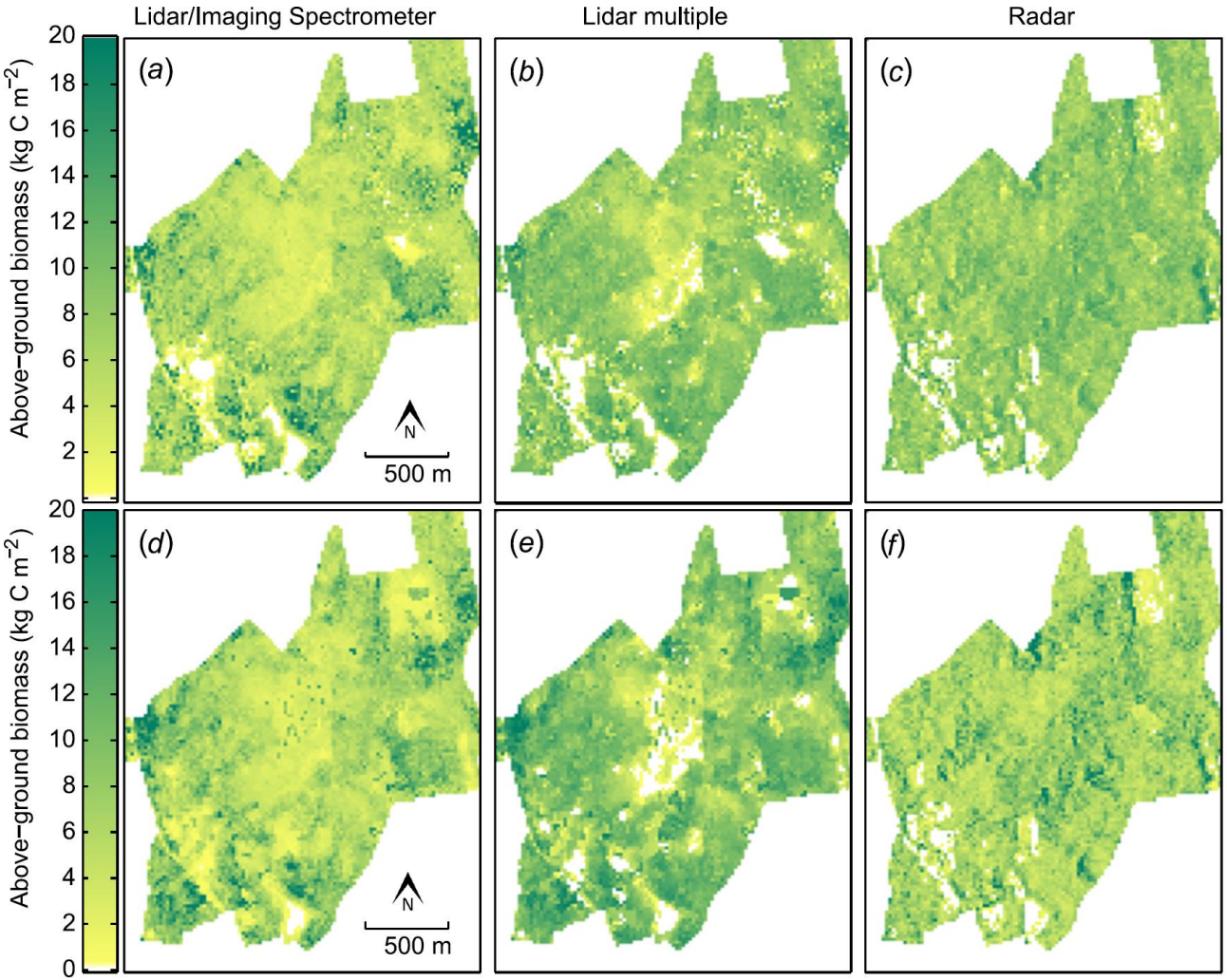

Figure 3. Spatial Distribution of Above-Ground Biomass (kgC m^{-2}) across the Prospect Hill Tract at Harvard Forest. (a/d) Lidar and imaging spectroscopy fusion method for deriving AGB for years 2003 (a) and for 2009 (d). (b/e) Lidar multiple regression method for deriving AGB for years 2003 (b) and for 2009 (e). (c) Radar multiple polarisation regression for deriving AGB. (f) Radar single polarisation regression for deriving AGB. The bottom left coordinates of the images are 42.5253, -72.1958.

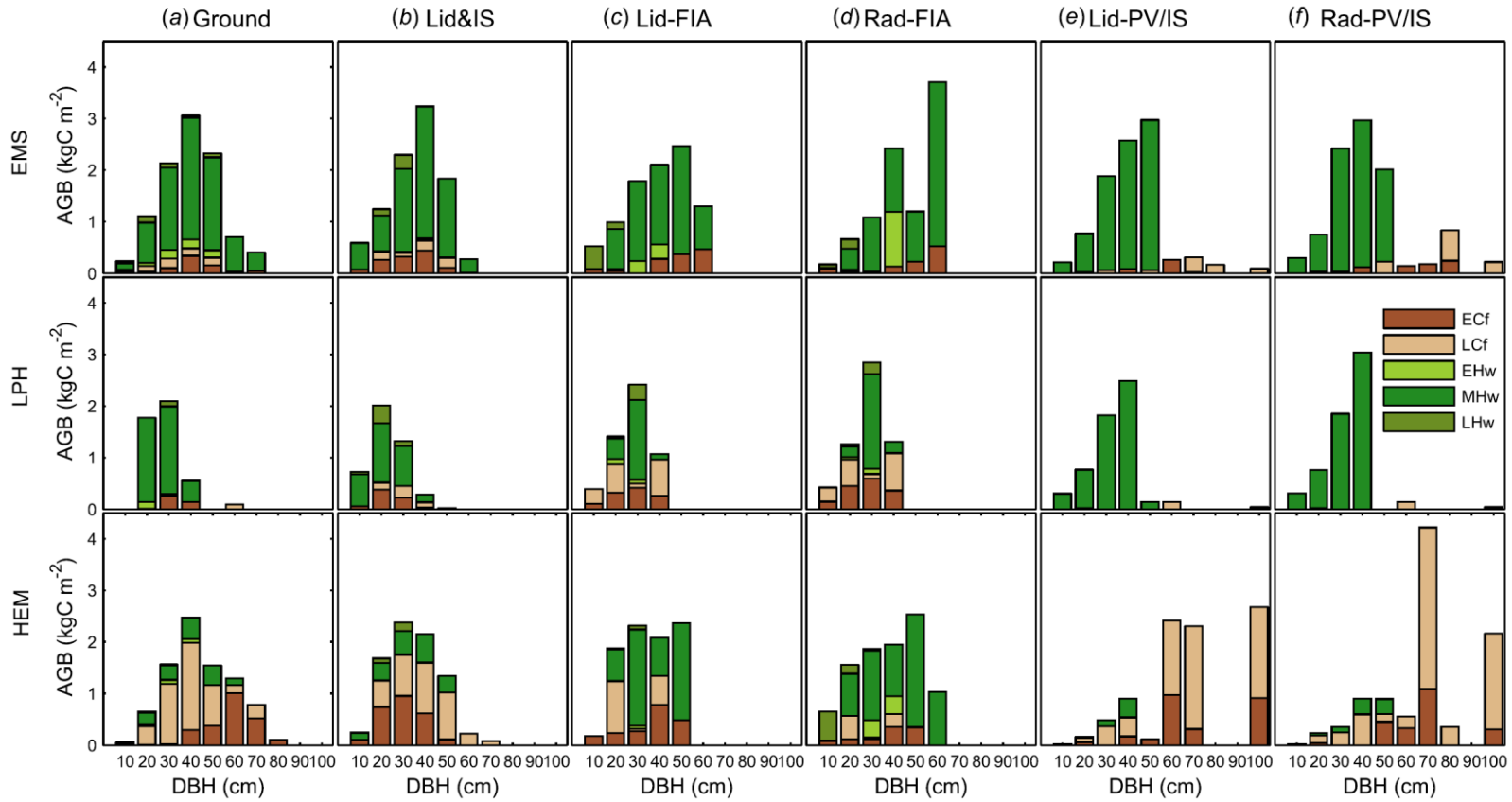

Figure 4. Initial Forest structure and composition presented as AGB size class distributions. These are for the Ground inventories (a), Lidar and imaging spectroscopy fusion method (b), Lidar (c) and Radar (d) links with FIA, and Lidar (e) and Radar (f) links with potential vegetation outputs and imaging spectroscopy. These are around the EMS (top row), LPH (middle row), and HEM (bottom row) flux towers at Harvard Forest. The plant functional types are early, mid, and late-successional hardwoods (EHw, MHw, LHw), and early, late-successional conifers (ECf, LCf).

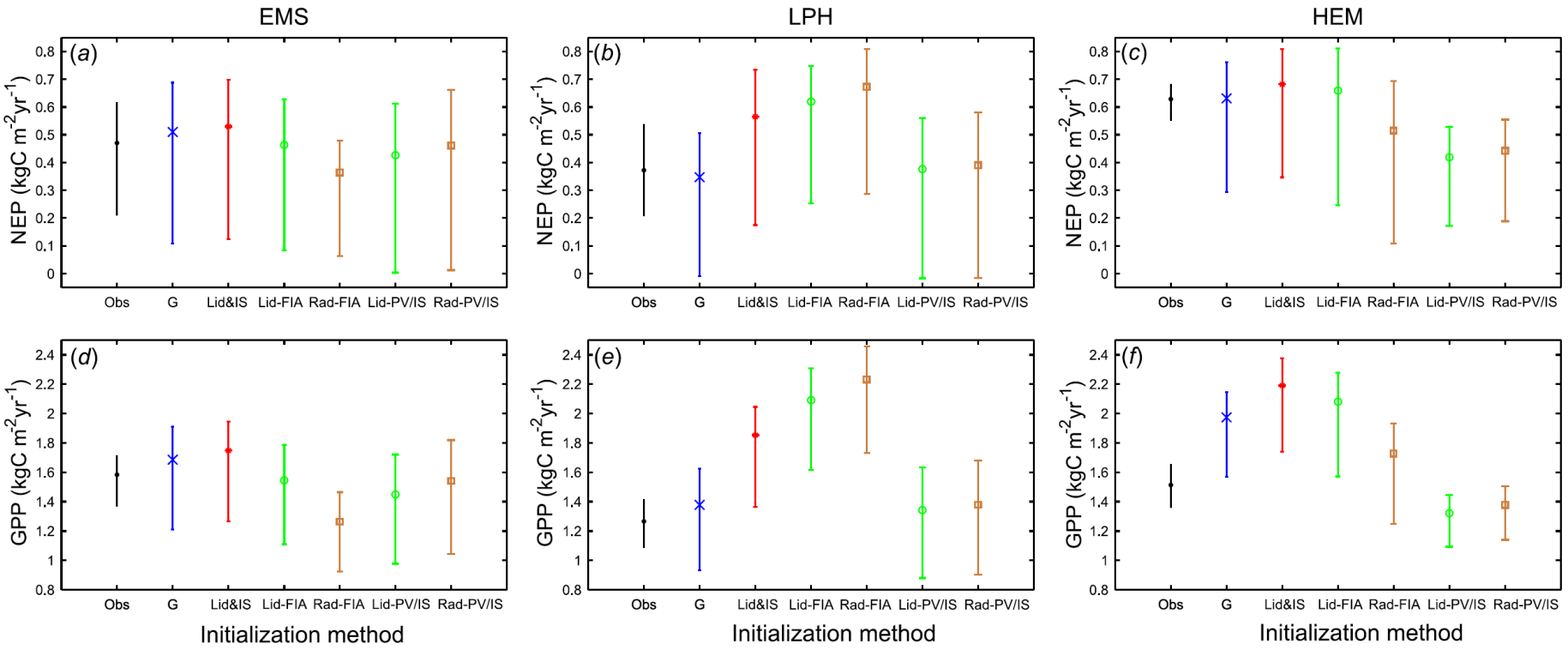

Figure 5. Carbon flux predictions at Harvard Forest using the five remote sensing-derived initial condition methods. Specifically, these are 6 year average (2003-2009) and inter-annual net ecosystem (NEP; a-c) and gross primary productivity (GPP; d-f) for the EMS (a,d), LPH (b,e), and HEM (c,f) flux towers from the ED2 terrestrial biosphere model simulations initialised using ground (G), lidar/imaging spectroscopy (Lid&IS), Lidar and Radar AGB links with FIA (Lid-FIA & Rad-FIA), and Lidar and Radar AGB links with potential vegetation outputs and imaging spectroscopy (Lid-PV/IS & Rad-PV/IS). Flux tower observations are also presented (Obs).

Supplementary Material

This section provides information on a) seasonal carbon flux uncertainty as opposed to just yearly data in the main body of the text ; b) resulting initial conditions and carbon fluxes linking multiple PFT potential vegetation output with lidar and radar derived above-ground-biomass distributions.

Table S1. Seasonal (monthly) net ecosystem and gross primary productivity RMSEs from the ground inventory-initialisations, predicted at the scale of the flux tower footprints in the vicinity of the EMS, HEM and LPH towers for the various initialisation methods Lid&IS (Lidar and Imaging Spectroscopy fusion), Lid-FIA & Rad-FIA (Lidar and Radar AGB links with FIA), and Lid-PV/IS & Rad-PV/IS (Lidar and Radar AGB links with potential vegetation outputs and imaging spectroscopy).

	GPP RMSE (kg C m^{-2} $month^{-1}$)				NEP RMSE (kg C m^{-2} $month^{-1}$)			
Method	**EMS**	**LPH**	**HEM**	**All sites**	**EMS**	**LPH**	**HEM**	**All sites**
Lid&IS fusion	0.012	0.047	0.021	**0.027**	0.011	0.026	0.008	**0.015**
Lid-FIA	0.014	0.081	0.050	**0.048**	0.006	0.052	0.047	**0.035**
Rad-FIA	0.047	0.094	0.077	**0.072**	0.026	0.058	0.072	**0.052**
Lid-PV/IS	0.024	0.011	0.065	**0.033**	0.011	0.011	0.028	**0.017**
Rad-PV/IS	0.019	0.014	0.059	**0.031**	0.013	0.014	0.025	**0.018**

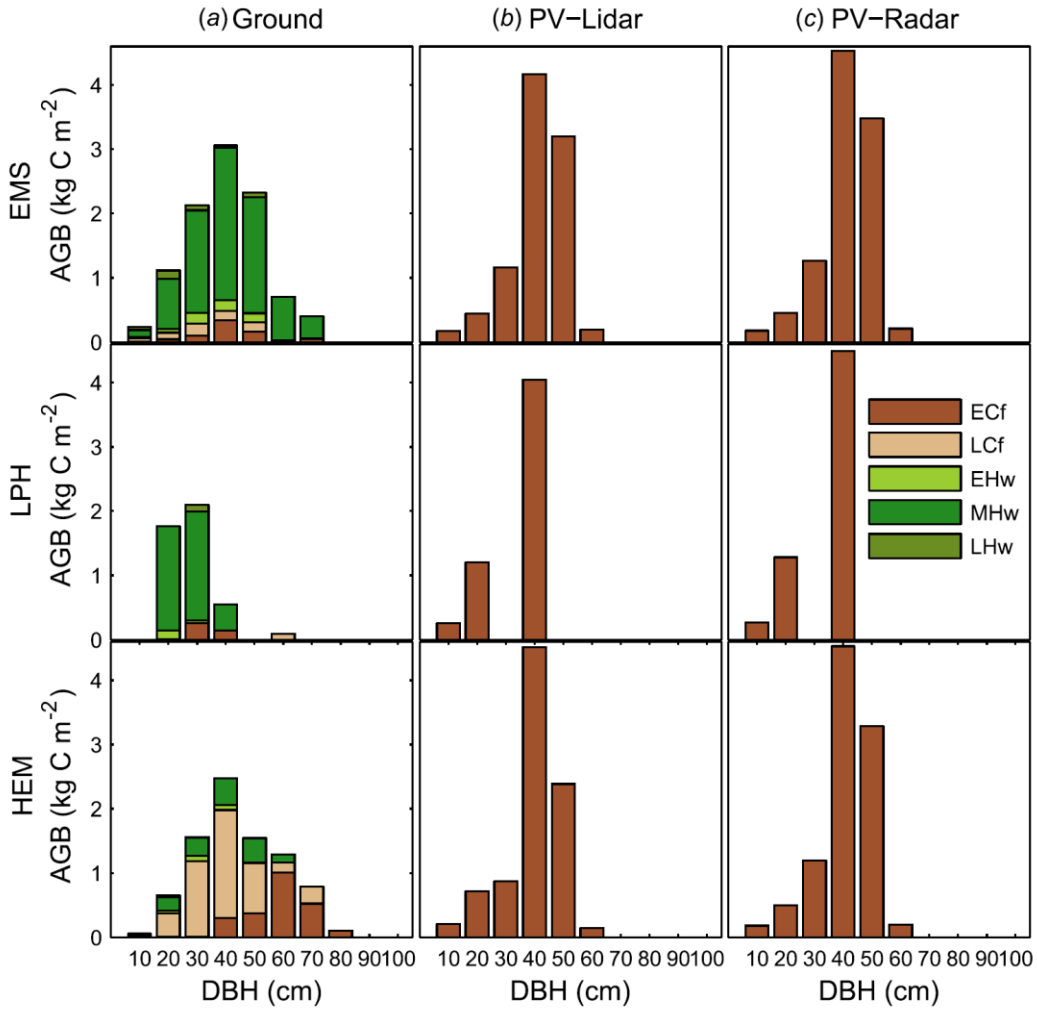

Figure S1. Initial Forest ecosystem structure and composition presented as above-ground biomass size class distributions for the Ground inventories (a), and Lidar (b) and Radar (c) AGB adjusted output from Potential Vegetation runs around the EMS (top row), LPH (middle row), and HEM (bottom row) flux towers at Harvard Forest. The Potential Vegetation runs were initialised with all PFTs, but early-successful conifers out-competed the other PFTs within 100 years.

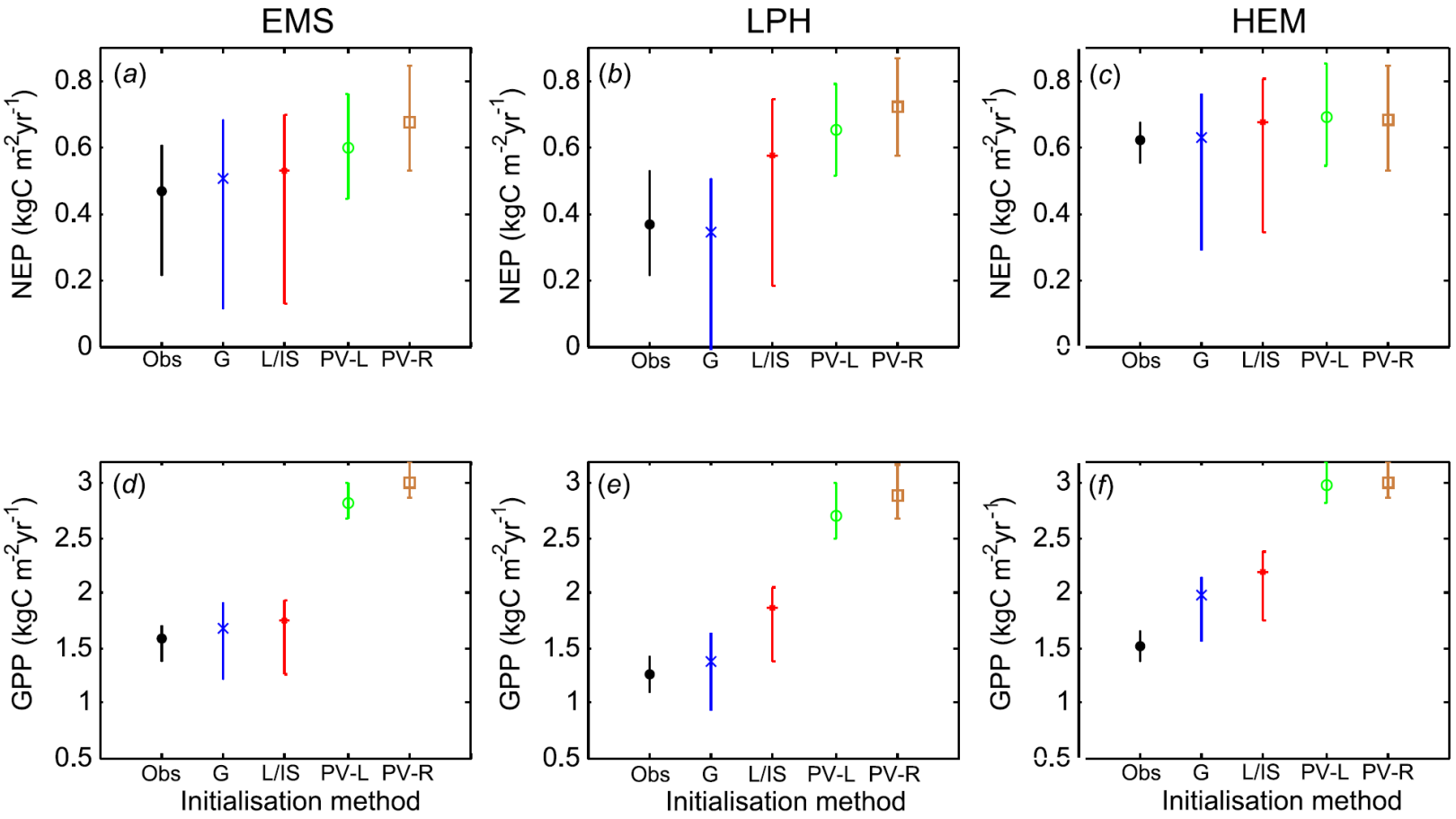

Figure S2. 6 year (2003-2009) average and inter-annual net ecosystem (NEP; a-c) and gross primary productivity (GPP; d-f) for the EMS (a,d), LPH (b,e), and HEM (c,f) flux towers from the ED2 terrestrial biosphere model simulations initialised using ground (G), lidar/imaging spectroscopy (L/IS), and Lidar and Radar AGB adjusted output from Potential Vegetation runs (PV-L & PV-R)